RESEARCH ARTICLE

ADVANCED OPTICAL MATERIALS
www.advopticalmat.de

Hybrid Plasmonic Coupled-Mode Metasurface Design for Shot-Noise Limited Ppb-Level Hydrogen Detection

*Mojie Luo, Hongki Lee, Junxiang Zhao, Jie Hu, Soojeong Baek, and Zhaowei Liu**

Plasmonic hydrogen sensors have enabled hydrogen detection below parts-per-million (ppm) range by boosting the sensitivity using localized surface plasmonic resonant (LSPR) structures. However, the intrinsic optical losses of Palladium (Pd), the primary plasmonic metal used for hydrogen detection, result in a low quality (Q) factor LSPR, which fundamentally hinders further improvement. In this work, a hybrid plasmonic metasurface is proposed that couples Pd-based LSPR structure with an Au film supporting surface plasmon polariton mode (Au-SPP). The coupled near-perfect absorber resonance yields a spectrally narrow, high Q response that retains strong sensitivity to hydrogen while improving resonance localization. Numerical analysis shows that, under shot-noise-limited conditions, the limit of detection (LoD) can be improved by over threefold compared to the state-of-the-art designs. This hybrid plasmonic coupled-mode metasurface thus presents a promising pathway to achieve parts-per-billion-level (ppb-level) hydrogen detection with enhanced spectral precision and robustness.

1. Introduction

Hydrogen has been widely accepted as a source of clean and sustainable energy, offering an alternative to fossil fuels, which have brought about severe environmental challenges. However, the production, storage, and transportation of hydrogen gas present safety risks, particularly due to its high diffusivity and flammability. The small molecular size of hydrogen makes it prone to leakage, underscoring the need for real-time monitoring and early detection to ensure safe deployment of hydrogen energy technologies.

Recently, detection of hydrogen at ppb concentrations has attracted increasing attention, enabling early identification of hydrogen leakage before it reaches hazardous levels. Although numerous hydrogen sensing technologies have been developed – including electrochemical,[1–3] thermal,[4,5] electrical,[6–9] and optical methods,[10–13] most of them have a LoD at the same order of the explosive threshold (0.1–4%). Achieving ppb-level detection requires orders-of-magnitude-higher sensitivity and sensing stability, rendering many conventional approaches inadequate. Among existing technologies, electrical and optical hydrogen sensing methods exhibit the lowest LoD and best stability.[14–16] Optical hydrogen sensors have advantages such as immunity to electrical sparks and compatibility with room-temperature operation. However, their sensitivity and response time at the ppb level are still far behind their electrical counterparts.

Plasmonic optical sensors based on Pd have emerged as prominent candidates due to their high sensitivity. These sensors operate by detecting either shifts in resonance frequency. Δ_{H_2} ω or changes in extinction Δ_{H_2} I, both caused by variations in the dielectric function of Pd as it absorbs hydrogen. Pd is an indispensable plasmonic component as it can reversibly form hydrides at room temperature. Two phase transitions occur during PdHx formation, where x denotes the atomic ratio of hydrogen to palladium. At low hydrogen pressure, a pure α phase (x<≈0.02) exists. As the pressure increases, an intermediate phase emerges and transitions into a β phase (x>≈0.6). The complete formation of PdH occurs when all interstitial sites of the face-centered cubic crystalline structure are filled by H atoms. During the transitions, the bulk plasmon energy of PdHx decreases from 7.7 eV ($x = 0$) to 4.3 eV (x = 1), as predicted by first-principles calculations.[17] Consequently, the dielectric function shifts toward lower energies, resulting in a red shift of plasmonic resonance wavelength $\Delta\lambda = \lambda(\mathrm{PdHx}) - \lambda(\mathrm{Pd})$.

Despite the potential of plasmonic hydrogen sensors for enhanced sensitivity, only a few nanostructure designs have been explored for ppm/ppb-level detection. For example, Pd/Au/Cu alloy nanoparticles with optimized compositions have achieved a LoD of 7 ppm in a vacuum condition.[18] Assemblies of Pd-coated polystyrene nanoparticles using gap-based LSPR have reached a LoD of 10 ppm in air and 2.5 ppm in Ar.[19] More recently, a metasurface composed of periodic Pd nanodisks has demonstrated a LoD as low as ≈250 ppb using inverse design strategies.[20] However, these approaches often sacrifice response time and durability to achieve high sensitivity. The primary bottleneck in plasmonic hydrogen sensors is the inherent optical loss in Pd that results in broadband resonances. This broadening creates a flat spectral response that is highly

M. Luo, H. Lee, J. Zhao, J. Hu, Z. Liu
Department of Electrical and Computer Engineering
University of California San Diego
La Jolla, CA 92093, USA
E-mail: zhaowei@ucsd.edu
S. Baek, Z. Liu
Center for Memory and Recording Research
University of California San Diego
La Jolla, CA 92093, USA

The ORCID identification number(s) for the author(s) of this article can be found under https://doi.org/10.1002/adom.202502036

DOI: 10.1002/adom.202502036

susceptible to noise, complicating the accurate localization of spectral shifts. As a result, even designs that achieve high sensitivity often suffer from poor temporal resolution and measurement uncertainty.

In this work, we propose a plasmonic hydrogen sensor based on a coupled plasmonic mode that approaches perfect absorption at the same time. The proposed design overcomes a fundamental limit in detection sensitivity existing in single-mode resonators by combining a lossy, low-Q sensing mode with a narrowband, high-Q probing mode. The high-Q probing mode can act as a spectral sampler that highlights the shifts of the low-Q sensing mode, significantly improving the spectral contrast while minimizing susceptibility to shot noise. We implement numerical simulations to demonstrate that these designs can improve LoD by more than threefold over the state-of-the-art optical sensor design. Our hybrid plasmonic metasurface provides an effective pathway to achieving ultra-sensitive, shot-noise-limited hydrogen detection in the ppb regime.

2. Principles and Design

2.1. Plasmonic Coupled Mode System

Optical refractive index sensors generally fall into two categories: indirect sensing and direct sensing. Indirect sensing involves detecting changes in the dielectric environment around a resonator, as commonly seen in many biosensing applications.[21,22] In contrast, direct sensing refers to detecting changes in the optical properties of the resonator material itself, which is the case of Pd-based plasmonic hydrogen sensors. The performance of a plasmonic resonator sensor can be evaluated by the figure-of-merit (FOM), defined as $|\Delta\omega/\mathrm{FWHM}|$. Regardless of direct or indirect sensing, for a single-mode resonator, there exists a fundamental limitation in the FOM. The first-order perturbation[23] of the resonance frequency shift caused by a small change in permittivity $\Delta\epsilon_a$ within the volume of the analyte V_a is given by

$$\Delta\omega = -\frac{\omega_0 \int_{V_a} d^3r\ \Delta\varepsilon_a |E(r)|^2}{2\int d^3r\varepsilon(r)|E(r)|^2} + o\left(\Delta\varepsilon_a^3\right) \tag{1}$$

where ω_0 is the resonant frequency, $\epsilon(r)$ is the spatial distribution of the permittivity, $\Delta\epsilon_a$ is the permittivity variation of the analyte, and $o(\Delta\varepsilon_a^3)$ denotes higher-order perturbations. The FWHM is determined by the total decay rate $\mathrm{FWHM} = 2(\gamma_r + \gamma_i)$, where γ_r is the radiative decay rate and γ_i is the intrinsic (non-radiative) decay rate. While γ_r does not have an analytical expression due to its dependence on the free-space coupling, γ_i can be given by

$$\gamma_i = \frac{\omega_0 \int d^3r\ \mathrm{Im}\ [\varepsilon(r)]|E(r)|^2}{2\int d^3r\varepsilon(r)|E(r)|^2} \tag{2}$$

Equations (1) and (2) are valid for low-loss and non-dispersive systems. However, in plasmonic devices, where the permittivity of the metal is usually negative, the denominator can become undefined. A more general perturbation theory has shown that the exact solution requires additional mathematical treatment that accounts for loss and dispersion.[24] Nevertheless, it has been shown that the correction to the numerator is empirically negligible and that to the denominator is not presented here since it will be cancelled out in the FOM. By substituting Equations (1) and (2) into FOM, and assuming $\gamma_r = \eta\gamma_i$, $(\eta > 0)$, we obtain

$$\mathrm{FOM} = \frac{\int_{V_a} d^3r\ |\Delta\varepsilon_a||E(r)|^2}{2(1+\eta)\int d^3r\ \mathrm{Im}\ [\varepsilon(r)]|E(r)|^2} \tag{3}$$

For indirect plasmonic-based sensing, FOM can be improved by shifting the optical near field from the lossy metallic components more toward the lossless analyte, simultaneously increasing the numerator and suppressing the denominator.[25,26] However, the analyte becomes the dominant source of loss for Pd-based direct sensing. As a result, the numerator and the denominator are coupled, making the improvement of the FOM extremely challenging. In this case, Equation (3) can be simplified into

$$\mathrm{FOM} = \frac{\int_{V_a} d^3r\ |\Delta\varepsilon_a||E(r)|^2}{2(1+\eta)\left(\int_{V_a} d^3r\ \mathrm{Im}\ [\varepsilon_a]|E(r)|^2 + \int_{V_{env}} d^3r\ \mathrm{Im}\ [\varepsilon_{env}(r)]|E(r)|^2\right)} = \frac{|\Delta\varepsilon_a|\int_{V_a} d^3r\,|E(r)|^2}{2(1+\eta)\ \mathrm{Im}\ [\varepsilon_a]\int_{V_a} d^3r|E(r)|^2} = \frac{|\Delta\varepsilon_a|}{2(1+\eta)\ \mathrm{Im}\ [\varepsilon_a]} \le \frac{|\Delta\varepsilon_a|}{2\ \mathrm{Im}\ [\varepsilon_a]} \tag{4}$$

The second equality holds when the environment surrounding the analyte is lossless, $\mathrm{Im}\,[\epsilon_{env}(\boldsymbol{r})] = 0$. This sets an upper limit of FOM due to the inherent loss in the analyte, regardless of resonator optimization. This limitation severely restricts the performance of Pd-based plasmonic hydrogen sensors at ppb-level detection.

To overcome this limitation, we propose a coupled-mode design integrating a low-Q sensing mode and a high-Q probing mode. The low-Q mode, such as Pd-LSPR, is represented by a shifting background in the spectrum, and we leverage the narrow bandwidth of the high-Q probing mode to assist in precise tracking of the low-Q resonance shift. To illustrate the mechanism of coupled modes, we implement an analysis using temporal coupled mode theory (TCMT).[27] We first consider a Lorentzian Pd-based resonator with a resonance frequency ω_0 and decay rate $\Gamma_0 = 2(\gamma_{r0} + \gamma_{i0})$, where γ_{r0} and γ_{i0} are radiative and dissipative decay rates, respectively. When hydrogen is absorbed, both the real and the imaginary parts of the permittivity of Pd change,

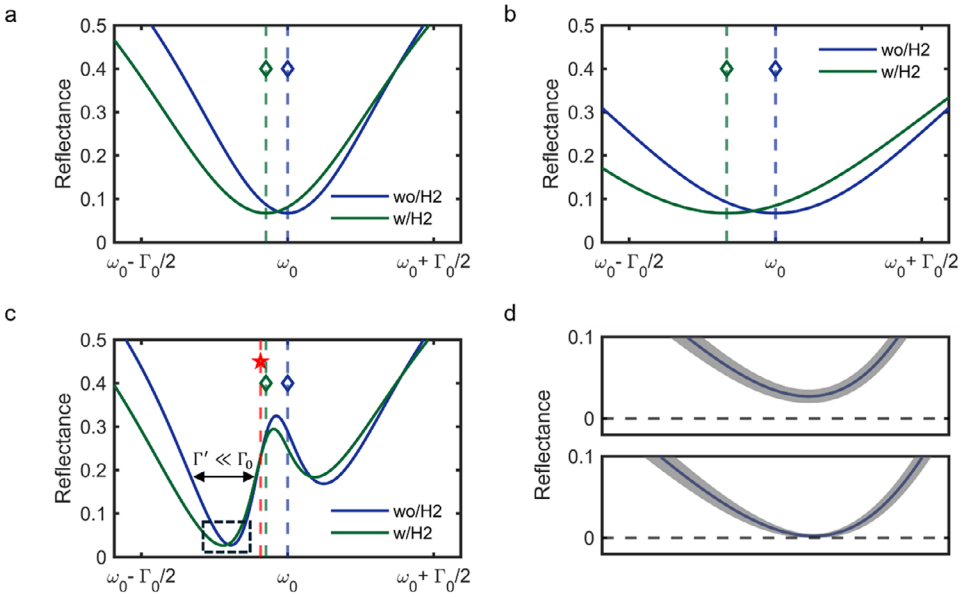

Figure 1. Comparison of hydrogen sensing spectra of single-mode and coupled modes. a) The reflectance spectra of the sensing mode with hydrogen sensitivity of $\Delta_{H_2}\omega_0$ and FWHM of Γ_0. The blue and green diamonds denote the position of the eigenfrequency of the low-Q sensing mode before and after hydrogen interaction. b) The reflectance spectra with doubled hydrogen sensitivity but doubled FWHM as well, leading to FOM pinning. c) The reflectance spectra of coupled mode resonance by introducing a high-Q probing resonance coupled with the same resonance defined in (a). The FWHM of the probing resonance is chosen as $\Gamma_c = \Gamma_0/10$ and the coupling strength is fixed as $u = \Gamma_0/3$. The red star denotes the eigenfrequency of the high-Q probing mode. d) Comparison of the spectra with shot noise before and after the perfect absorption design. The latter allows improved spectral localization. The shaded area represents the standard deviation of the shot noise.

resulting in a resonance frequency shift $\Delta_{H_2}\omega_0$, as shown in **Figure** 1a. Figure 1b highlights that increasing the sensitivity $\Delta_{H_2}\omega_0$, whether by scaling up,[25] or optimizing the geometry, also increases the FWHM nearly proportionally. This behavior aligns with the prediction of Equation (4). To design the coupled mode system, we introduce a high-Q mode to the low-Q mode, which has a resonant frequency of ω_c and much narrower linewidths of γ_{rc}, γ_{ic}. The full spectral response of the coupled system is described by TCMT equations (Equations S1-S6, Supporting Information) as

$$R(\omega) = \left| -1 + 2i \frac{\gamma_{rc}\left(\omega - \omega_0 + i\gamma_{i0}\right) + \gamma_{r0}\left(\omega - \omega_c + i\gamma_{ic}\right) - 2u\sqrt{\gamma_{r0}\gamma_{rc}}}{\left(\omega - \omega_0 + i\left(\gamma_{r0} + \gamma_{i0}\right)\right)\left(\omega - \omega_c + i\left(\gamma_{rc} + \gamma_{ic}\right)\right) - \left(u + i\sqrt{\gamma_{r0}\gamma_{rc}}\right)^2} \right|^2 \quad (5)$$

where u represents the coupling strength that is often dependent on modal overlap. When the coupling is sufficiently strong, the spectrum exhibits two hybridized modes—a phenomenon known as avoided crossing[28]—corresponding to the two dips shown in Figure 1c. Here, the hybridized modes not only inherit the sensitivity of the original low-Q mode, but also dramatically enhance spectral localization by achieving much narrower linewidths, significantly improving the FOM. Importantly, frequency detuning of the two modes can be engineered such that the spectral shift is mainly expressed by one of the reflectance dips, allowing for single-dip Lorentzian fitting and therefore reducing spectral readout complexity.

2.2. Perfect Absorber

Although the coupled mode system can significantly narrow the spectral linewidth, the spectral shift under ultra-low hydrogen concentrations (below ppm) remains in the sub-nanometer range that is orders of magnitude smaller than FWHM. Consequently, Pd-LSPR, even when in the hybrid system, still suffers from shallow spectral gradients near the reflection minimum. This limits the precision, especially since shot noise introduces fluctuations in spectral dip localization even if dark noises such as Johnson–Nyquist noise and read-out noise are eliminated by hardware and electronics optimization. To address this issue, we further propose introducing the perfect absorption condition to our hybrid coupled-mode design. This will suppress the shot-noise-induced spectral fluctuation of the system. Figure 1d shows the spectrum with simulated shot noise, comparing cases with and without a perfect absorption design (zoomed into the dashed

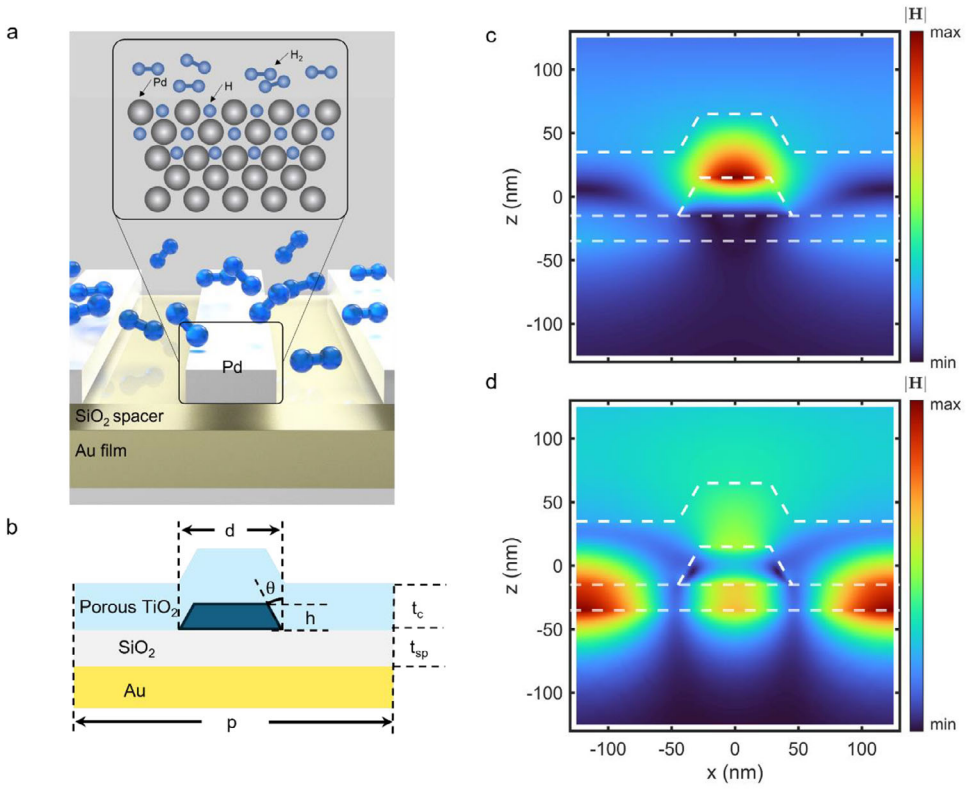

Figure 2. Schematic of Pd-Au plasmonic hybrid metasurface for hydrogen detection. a) Schematic of the metasurface based on a 1D sub-diffraction grating. The grating consists of Pd ridges that support the sensing mode LSPR, with a dipolar orientation along the grating direction. b) The geometry of one unit cell, including a TiO_2 cover layer, a SiO_2 spacer, and an Au mirror. c) Magnetic profile $|\boldsymbol{H}|$ of coupled Pd-LSPR. d) Magnetic field profile $|\boldsymbol{H}|$ of coupled Au-SPP. The anti-phase magnetic maximum lobes at the center and in between the ridges originate from the interference of oppositely travelling SPP ($\pm \boldsymbol{k_G}$).

box in Figure 1c). The shot noise in a normalized reflectance measurement is given by

$$\sigma_s = \frac{\sqrt{N_{\text{total}} R}}{N_{\text{total}}} = \sqrt{\frac{R}{N_{\text{total}}}} \tag{6}$$

where σ_s is the standard deviation of shot noise normalized to total photon arrival counts N_{total}, and R denotes reflectance. By engineering the structure to achieve near-zero reflectance at the dip, we can minimize shot noise at the spectral region of interest, which results in a significant improvement in spectral readout precision.

3. Results

To prove the concept, we design a hybrid plasmonic metasurface composed of a Pd grating on an Au substrate, separated by a fused silica spacer and covered by a TiO_2 layer (**Figure 2a**). The porous TiO_2 cover layer, potentially enabled by colloidal or nanoporous TiO_2 films, has been previously demonstrated to be effective for rapid hydrogen permeation when used as a protective self-cleaning coating.[29,30] In our design, we leverage the high refractive index of TiO_2 at the visible frequency to align the resonant frequency of coupled modes. The thickness of Pd and TiO_2 is limited to 30 and 50 nm, respectively, to ensure fast hydrogen absorption and desorption kinetics for practical applications. The periodic grating, the ridge of each supporting electric-dipolar LSPR, folds Au-SPP into the first Brillouin zone and yields a coupled mode system. Figure 2b shows the geometry of our unit cell design, where t_{sp} denotes the thickness of the fused silica spacer, h and d denote the height and width of the Pd ridge, p denotes the period, and t_c denotes the thickness of the TiO_2 cover layer. The Pd ridge is modeled with a side wall of tilt angle 25° along with the cover layer to approximate common fabrication conditions. Numerical simulations are performed using the frequency-domain finite element method of the commercially available software COMSOL. The magnetic field |H| profile of Pd-LSPR and Au-SPP after coupling is shown in Figure 2c,d, respectively. The dual anti-phase magnetic field lobes at the interface of Au are the interference pattern of 1st-order BZ-folded surface wave traveling in opposite directions ($k_{||} = \pm 2\pi/\text{p}$), and the plasmonic origin of the surface wave marks itself SPP.

Figure 3a presents the band diagram of the hybrid structure, showing the coupling band between Pd-LSPR and Au-SPP. The right half of the map is calculated based on pure Pd, and the left half corresponds to $PdH_{0.125}$. The dielectric functions of Pd and PdH_x are adapted from the work of Silkin et al.[17] The black dashed line guides the trajectory of Au-SPP and is calculated by eigenfrequency analysis. We use $PdH_{0.125}$ as the lowest

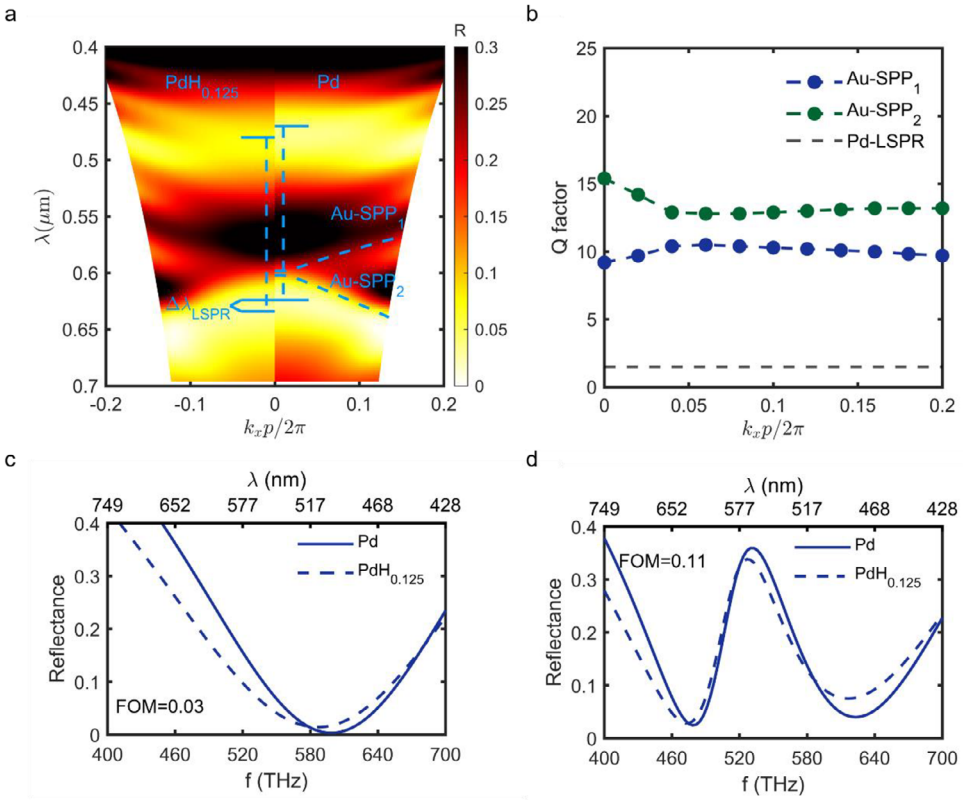

Figure 3. Band structure and mode analysis of plasmonic coupled-mode metasurface. a) Band structure. The right half uses Pd and the left half uses $PdH_{0.125}$. The black dashed line represents the eigenfrequency trajectory of the folded Au-SPP. b) Calculated Q factor of Au-SPP and Pd-LSPR eigenmodes. c) Retrieved single-mode Pd-LSPR spectra by TCMT fitting. d) Coupled mode spectra. The calculated FOM of the low-frequency dip indicates more than 3x improvement over Pd-LSPR. Both are operating at a normal incident angle.

hydrogenated composition in our simulation, corresponding to ≈1% H_2 at room temperature based on pressure–composition isotherms of PdH_x systems. This value is chosen because it is the lowest PdH_x composition for which the dielectric function has been reported in the literature, and we use it as a benchmark to characterize the sensing performance. Figure 3b shows the Q factor of Au-SPP and Pd-LSPR. As the two branches of Au-SPP fold at the Γ point, degenerate splitting occurs, producing one branch with vanishing radiative decay rate (Au-SPP_2), and another with finite radiative linewidth (Au-SPP_1) that is excitable under normal incidence. This has been observed and theoretically analyzed in a more general system.[31,32] The Q factor of the radiative branch is nearly an order of magnitude higher than that of Pd-LSPR owing to strong near-field localization in the gap between the Pd grating and the Au substrate.

Pd-LSPR exhibits lower Q due to significant intrinsic absorption in Pd. Its resonance is primarily influenced by the grating width and the TiO_2 cover layer thickness. Importantly, the Pd-LSPR mode undergoes a redshift ($\Delta_{H_2}\omega < 0$) upon hydrogenation, forming the basis for hydrogen sensing. Due to the narrowband nature of the probing mode, the effective FWHM of the spectral features is greatly reduced, leading to a significant enhancement in the FOM. Figure 3c,d compares the spectra of the standalone Pd-LSPR and the coupled mode with parameters retrieved through TCMT fitting. The resonance shift $\Delta_{H_2}\omega_0$ and FWHM are 72 and 2314 for Pd-LSPR, and 44 and 408 for the low-frequency dip of the hybrid mode, in units of rad THz. The comparison reveals that the hybrid spectrum exhibits a more than threefold improvement in FOM compared to the uncoupled Pd-LSPR mode. This demonstrates the efficacy of the coupled-mode approach in enhancing spectral resolution without significantly compromising sensitivity.

For plasmonic hydrogen sensing, where reflectance or transmittance spectrum is measured by optical detection setups using commercial light sources, spectrometers, and cameras, shot noise is the dominant noise source. To mitigate the impact of shot noise on spectral localization, we focus on optimizing the reflectance dip on the low-frequency side, as it experiences a larger spectral shift due to frequency detuning between the Pd-LSPR and Au-SPP modes. **Figure** 4a shows the effect of varying the grating ridge width d. Increasing d enhances the radiative decay rate of the folded Au-SPP,[32] which deepens the reflectance dip and achieves perfect absorption (Figure S1, Supporting Information). Figure 4b,c compares the reflectance spectrum of two coupled mode configurations, one near the perfect absorption condition ($R(\lambda_{dip}) = 0.005$) and one with a higher minimum reflectance ($R(\lambda_{dip}) = 0.1$), both assuming a N_{total} of 10^6 within the spectral resolution. The insets highlight the resonance dips under identical noise conditions, respectively. The spectra with near-zero reflectance clearly show superiorly reduced spectral fluctuations. We note that whilst the intensity is weakest at the minimum reflectance, a shot-noise-limit condition can still

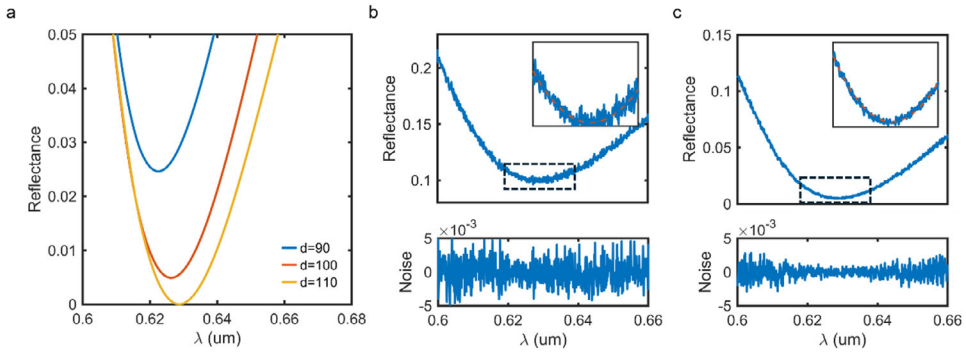

Figure 4. Perfect absorber design a) Reflectance with varying grating width. The other parameters are fixed, given by h = 30 nm, tc = 50 nm, tsp = 20 nm. Top: Reflectance spectra with shot noise. b) when the minimum reflectance is 0.1 c) when the minimum reflectance is 0.005. Bottom: Implemented normalized shot noise. Inset: Magnified view of the dip, where noise-induced fluctuations dominate the spectral localization uncertainty.

be maintained with strong illumination power (Figure S2, Supporting Information). By engineering the grating ridge width, the reflectance minimum can also be tuned to accommodate practical photon budgets.

LoD represents the lowest analyte concentration that gives a reliably measurable signal, defined as $3\sigma_{\lambda_{\mathrm{dip}}}/\frac{\delta\lambda_{\mathrm{dip}}}{\delta[\mathrm{H}_2]}$, where $\sigma_{\lambda_{\mathrm{dip}}}$ is the spectral localization uncertainty of the dip, and $\frac{\delta\lambda_{\mathrm{dip}}}{\delta[\mathrm{H}_2]}$ is the responsivity. However, there is no closed-form analytic expression because $\sigma_{\lambda_{\mathrm{dip}}}$ is implicitly dependent on both the fitting method and noises, and $\frac{\delta\lambda_{\mathrm{dip}}}{\delta[\mathrm{H}_2]}$ is not continuously accessible by numerical methods. To quantitatively evaluate the LoD under shot-noise-limited conditions, we perform a statistical analysis on the value $\Delta_{\mathrm{H}_2}\lambda_{\mathrm{dip}}/\sigma_{\lambda_{\mathrm{dip}}}$, which is inversely proportional to LoD, based on Monte Carlo simulations. We apply 500 instances of randomly generated shot noise to the reflectance spectrum and fit the dip position. $\Delta_{\mathrm{H}_2}\lambda_{\mathrm{dip}}$ is calculated as the difference between the fitted dip wavelengths of $\mathrm{PdH}_{0.125}$ and pure Pd: $\Delta_{\mathrm{H}_2}\lambda_{\mathrm{dip}} = \lambda_{\mathrm{dip}}(\mathrm{PdH}_{0.125}) - \lambda_{\mathrm{dip}}(\mathrm{Pd})$. The shot noise is normalized to a N_{total} of 10^6 at each spectral sample point, corresponding to an SNR of 30 dB at unity reflectance. **Figure** 5a shows the resulting $\Delta_{\mathrm{H}_2}\lambda_{\mathrm{dip}}/\sigma_{\lambda_{\mathrm{dip}}}$ with varying $R(\lambda_{\mathrm{dip}})$. The simulation confirms that dip localization becomes significantly more precise as the reflectance minimum approaches zero, resulting in improved LoD. In comparison, we numerically reproduce the design by Nugroho et al.20, which experimentally realized a 250 ppb LoD using an LSPR nanodisk array (Figure S3, Supporting Information). The result shows that LSPR resonators, after optimization, correspond to a $\Delta_{\mathrm{H}_2}\lambda_{\mathrm{dip}}/\sigma_{\lambda_{\mathrm{dip}}}$ value of ≈700 applying equivalent noise conditions. Therefore, our hybrid coupled-mode design with near-perfect absorption demonstrates a potential of more than threefold improvement over the state-of-the-art plasmonic hydrogen sensor, resulting in ppb-level LoD.

To further validate the robustness and generality of our approach, we conduct a parametric sweep over key structural parameters in the vicinity of our optimized design. Specifically, we vary the Pd ridge width d from 60 to 120 nm and period p from 250 to 300 nm. These parameters play a crucial role in defining the coupling strength between the Pd-LSPR and Au-SPP modes, and in tuning the radiative loss rate necessary to achieve perfect

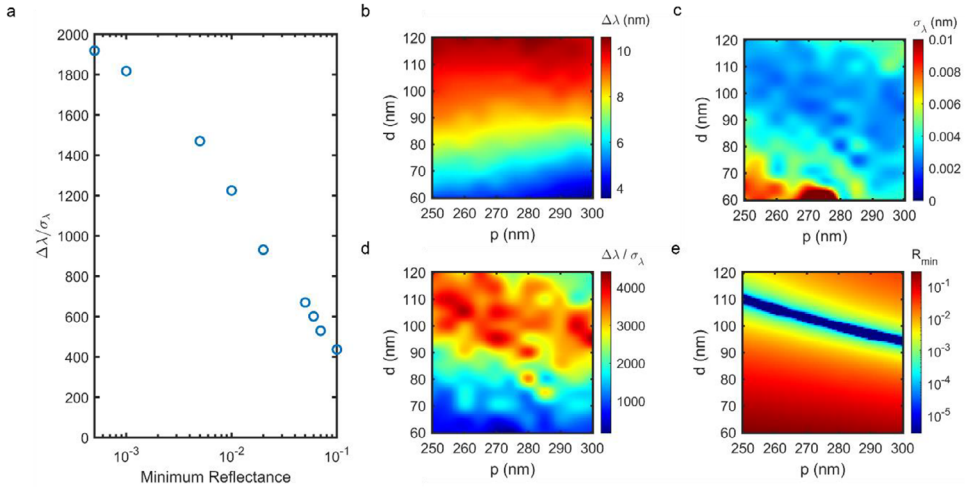

Figure 5. Sensor performance characterization and optimization. a) $\Delta\lambda/\sigma_\lambda$ with varying minimum reflectance. The design parameters are d = 110 nm, p = 250 nm, h = 30 nm, t_c = 50 nm, t_{sp} = 20 nm. b) $\Delta\lambda$, c) σ_λ, d) $\Delta\lambda/\sigma_\lambda$, and e) Reflectance minimum in the parameter space of period and ridge width. The optimal design with maximum $\Delta\lambda/\sigma_\lambda$ has the lowest LoD.

absorption. For each combination of (d,p), we compute $\Delta_{H_2}\lambda_{dip}$ (Figure 5b), $\sigma_{\lambda_{dip}}$ (Figure 5c), $\Delta_{H_2}\lambda_{dip}/\sigma_{\lambda_{dip}}$ (Figure 5d), and $R(\lambda_{dip})$ (Figure 5e). The results clearly show that $\Delta_{H_2}\lambda_{dip}/\sigma_{\lambda_{dip}}$ peaks in regions where the reflectance minimum is lowest. We can also observe a slight increase in $\Delta_{H_2}\lambda_{dip}$ as the structure scales up, consistent with previous findings that larger geometries can support higher sensitivity due to redshifted resonances at longer wavelengths.[25] However, this increase in sensitivity is not sufficient to ensure better LoD because the resonance linewidth also broadens at longer wavelength. Importantly, the parameter space around the optimum forms a broad, continuous region of high performance, rather than a narrow peak. This suggests that the design is fabrication-tolerant, allowing for small variations in ridge width or period without significantly compromising LoD. Such robustness is essential for practical implementation.

4. Conclusion

In this work, we present a hybrid plasmonic metasurface sensor that combines Pd-LSPR with a high-Q Brillouin-zone-folding Au-SPP to achieve shot-noise-limited hydrogen detection at ppb levels. By leveraging the coupled-mode framework, our design preserves the strong sensitivity of Pd-LSPR while introducing sharp, narrowband features through high-Q spectral sampling, which enhances spectral localization and boosts the effective FOM. To overcome the intrinsic linewidth and noise limitations of lossy Pd-based sensors, we implement the perfect absorption condition, which suppresses the reflectance near the resonance dip and minimizes the impact of shot noise. We quantitatively demonstrate that this strategy yields over a threefold improvement in limit of detection compared to state-of-the-art plasmonic hydrogen sensors under equivalent noise assumptions. Finally, we emphasize that our design can also be generalized to other material systems, such as replacing the coating layer with PMMA and PTFE, which also support H_2 diffusion kinetics. TiO_2 features a high refractive index of ≈2.3 in the visible frequency. Should the TiO_2 be substituted by other low-index materials, such as PMMA (with a lower refractive index of ≈1.5), our design can still be achieved by fine-tuning additional geometrical degrees of freedom, such as the material and thickness of the spacer layer. Our sensor architecture offers a promising route to simultaneously achieve ultralow detection limits, fast response times, and long-term durability, making it a strong candidate for next-generation hydrogen safety and environmental monitoring systems.

We recognize several promising directions for future exploration beyond the current work. In the design section, TCMT was employed to analyze mode coupling dynamics, but not directly used to track spectral shifts. However, the current fitting methods do not capture the full structure of the coupled mode spectrum and can potentially lead to associated loss of information due to the empirical nature of Lorentzian fitting. In the future, fitting methods based on TCMT could be developed to incorporate parameters such as resonant frequencies and mode decay rates that are physically normalized and easier to regularize, making the model well-suited for robust spectral characterization. Additionally, while our analysis revealed a fundamental FOM bottleneck for single-mode Lorentzian resonators in wavelength-shift-based detection, this limitation can be circumvented by other hybrid designs. Specifically, the imaginary part of the permittivity change $\mathrm{Im}[\Delta\epsilon_a]$, which contributes to system loss, can be exploited in alternative detection schemes. A compelling example is the use of exceptional point[33] sensing, achieved by coupling two lossy modes. Perturbing the loss in one mode breaks the loss balance and induces a sharp transition in the behavior of light transport, potentially leading to an extremely large signal readout even at low hydrogen concentration. Furthermore, the concept underlying our coupled-mode approach can be extended to different sensing platforms other than free-space optics. For instance, hybrid platforms that integrate photonic crystals with plasmonic nanorods,[34] or combine waveguides with plasmonic ring resonators,[35] could leverage similar principles to enhance sensitivity and noise resilience. These opportunities open a broader landscape for implementing coupled-mode designs across diverse sensing platforms.

Supporting Information

Supporting Information is available from the Wiley Online Library or from the author.

Acknowledgements

This work was supported by Advanced Research Projects Agency–Energy (Grant No. DE-AR0001985).

Conflict of Interest

The authors declare no conflict of interest.

Data Availability Statement

The data that support the findings of this study are available from the corresponding author upon reasonable request.

Keywords

coupled modes, hydrogen, limit of detection, metasurface, plasmonics, sensors

Received: June 26, 2025
Revised: August 28, 2025
Published online:

[1] G. Fadeyev, A. Kalakin, A. Demin, A. Volkov, A. Brouzgou, P. Tsiakaras, *Int. J. Hydrog. Energy* **2013**, *38*, 13484.
[2] L. P. Martin, A.-Q. Pham, R. S. Glass, *Solid State Ion* **2004**, *175*, 527.
[3] K. Arora, N. K. Puri, *Vacuum* **2018**, *154*, 302.
[4] I. Simon, M. Arndt, *Sens. Actuators Phys.* **2002**, *97–98*, 104.
[5] P. Tardy, J.-R. Coulon, C. Lucat, F. Menil, *Sens. Actuators, B* **2004**, *98*, 63.
[6] P. Pandey, J. K. Srivastava, V. N. Mishra, R. Dwivedi, *Solid State Sci.* **2009**, *11*, 1370.
[7] V. Krivetskiy, A. Efitorov, A. Arkhipenko, S. Vladimirova, M. Rumyantseva, S. Dolenko, A. Gaskov, *Sens. Actuators, B* **2018**, *254*, 502.

[8] H. Kim, Y. Pak, Y. Jeong, W. Kim, J. Kim, G. Y. Jung, *Sens. Actuators, B* **2018**, *262*, 460.
[9] K. Rajoua, L. Baklouti, F. Favier, *J. Phys. Chem. C* **2015**, *119*, 10130.
[10] S. Bao, K. Tajima, Y. Yamada, M. Okada, K. Yoshimura, *Sol. Energy Mater. Sol. Cells* **2008**, *92*, 224.
[11] A. Hosoki, M. Nishiyama, H. Igawa, A. Seki, Y. Choi, K. Watanabe, *Sens. Actuators, B* **2013**, *185*, 53.
[12] R. J. Westerwaal, J. S. A. Rooijmans, L. Leclercq, D. G. Gheorghe, T. Radeva, L. Mooij, T. Mak, L. Polak, M. Slaman, B. Dam, T. h. Rasing, *Int. J. Hydrog. Energy* **2013**, *38*, 4201.
[13] Y. Liu, N. Zhang, P. Li, S. Bi, X. Zhang, S. Chen, W. Peng, *Sens. Actuators, B* **2019**, *301*, 127136.
[14] M. Darabpour, M. M. Doroodmand, *IEEE Sens. J.* **2015**, *15*, 2391.
[15] J. Hu, Y. Sun, Y. Xue, M. Zhang, P. Li, K. Lian, S. Zhuiykov, W. Zhang, Y. Chen, *Sens. Actuators, B* **2018**, *257*, 124.
[16] F. A. A. Nugroho, I. Darmadi, L. Cusinato, A. Susarrey-Arce, H. Schreuders, L. J. Bannenberg, A. B. da Silva Fanta, S. Kadkhodazadeh, J. B. Wagner, T. J. Antosiewicz, A. Hellman, V. P. Zhdanov, B. Dam, C. Langhammer, *Nat. Mater.* **2019**, *18*, 489.
[17] V. M. Silkin, R. Díez Muiño, I. P. Chernov, E. V. Chulkov, P. M. Echenique, *J. Phys. Condens. Matter* **2012**, *24*, 104021.
[18] I. Darmadi, F. A. A. Nugroho, S. Kadkhodazadeh, J. B. Wagner, C. Langhammer, *ACS Sens.* **2019**, *4*, 1424.
[19] H. M. Luong, M. T. Pham, T. Guin, R. P. Madhogaria, M.-H. Phan, G. K. Larsen, T. D. Nguyen, *Nat. Commun.* **2021**, *12*, 2414.
[20] F. A. A. Nugroho, P. Bai, I. Darmadi, G. W. Castellanos, J. Fritzsche, C. Langhammer, J. Gómez Rivas, A. Baldi, *Nat. Commun.* **2022**, *13*, 5737.
[21] R. A. Mahmud, R. H. Sagor, M. Z. M. Khan, *Opt. Laser Technol.* **2023**, *159*, 108939.
[22] S. Verma, A. K. Pathak, B. M. A. Rahman, *Micromachines* **2024**, *15*, 502.
[23] *Photonic Crystals: Molding the Flow of Light*, 2nd ed., (Ed.: J. D. Joannopoulos, S. G. Johnson, J. N. Winn, R. D. Meade), Princeton University Press, Princeton, **2008**.
[24] A. Raman, S. Fan, *Phys. Rev. B* **2011**, *83*, 205131.
[25] F. A. A. Nugroho, I. Darmadi, V. P. Zhdanov, C. Langhammer, *ACS Nano* **2018**, *12*, 9903.
[26] S. Tang, C. Chang, P. Zhou, Y. Zou, *Photonics* **2022**, *9*, 224.
[27] W. Suh, Z. Wang, S. Fan, *IEEE J. Quantum Electron.* **2004**, *40*, 1511.
[28] J. Y. Kim, J. Park, G. R. Holdman, J. T. Heiden, S. Kim, V. W. Brar, M. S. Jang, *Nat. Commun.* **2022**, *13*, 2103.
[29] Y. Paz, Z. Luo, L. Rabenberg, A. Heller, *J. Mater. Res.* **1995**, *10*, 2842.
[30] J. R. Pitts, P. Liu, R. D. Smith, Photo-Oxidation Catalysts, US7560409B2, July 14, 2009, https://patents.google.com/patent/US7560409B2/en?oq=US+7%2c560%2c409+B2 (accessed: March 2025).
[31] P. Hu, J. Wang, Q. Jiang, J. Wang, L. Shi, D. Han, Z. Q. Zhang, C. T. Chan, J. Zi, *Optica* **2022**, *9*, 1353.
[32] L. Huang, R. Jin, C. Zhou, G. Li, L. Xu, A. Overvig, F. Deng, X. Chen, W. Lu, A. Alù, A. E. Miroshnichenko, *Nat. Commun.* **2023**, *14*, 3433.
[33] J. Wiersig, *Photonics Res.* **2020**, *8*, 1457.
[34] L. Hajshahvaladi, H. Kaatuzian, M. Moghaddasi, M. Danaie, *Sci. Rep.* **2022**, *12*, 21292.
[35] M. A. Butt, S. N. Khonina, N. L. Kazanskiy, *J. Mod. Opt.* **2018**, *65*, 1135.